Biomedical Optics EXPRESS

Non-contact optical spectroscopy for tumor-sensitive diffuse reflectance and fluorescence measurements on murine subcutaneous tissue models: Monte Carlo modeling and experimental validations

MD ZAHID HASAN, PRANTO SOUMIK SAHA, MADISON O. KORFHAGE, AND CAIGANG ZHU[*]

Department of Biomedical Engineering, University of Kentucky, Lexington, KY 40506, USA
[*]*caigang.zhu@uky.edu*

Abstract: Fiber-optic probes are commonly used in biomedical optical spectroscopy platforms for light delivery and collection. At the same time, it was reported that the inconsistent probe-sample contact could induce significant distortions in measured optical signals, which consequently cause large analysis errors. To address this challenge, non-contact optical spectroscopy has been explored for tissue characterizations. However, existing non-contact optical spectroscopy platforms primarily focused on diffuse reflectance measurements and may still use a fiber probe in which the probe was imaged onto the tissue surface using a lens, which serves as a non-contact probe for the measurements. Here, we report a fiber-probe-free, dark-field-based, non-contact optical spectroscopy for both diffuse reflectance and fluorescence measurements on turbid medium and tissues. To optimize the system design, we developed a novel Monte Carlo method to simulate such a non-contact setup for both diffuse reflectance and fluorescence measurements on murine subcutaneous tissue models with a spherical tumor-like target. We performed Monte Carlo simulations to identify the most tumor-sensitive configurations, from which we found that both the depth of the light focal point in tissue and the lens numerical aperture would dramatically affect the system's tumor detection sensitivity. We then conducted tissue-mimicking phantom studies to solidify these findings. Our reported Monte Carlo technique can be a useful computational tool for designing non-contact optical spectroscopy systems. Our non-contact optical setup and experimental findings will potentially offer a new approach for sensitive optical monitoring of tumor physiology in biological models using a non-contact optical spectroscopy platform to advance cancer research.

© 2023 Optica Publishing Group under the terms of the Optica Open Access Publishing Agreement

1. Introduction

Optical spectroscopy has been explored extensively for various biomedical applications due to its non-invasiveness and capability to provide quantitative functional information on tissues in near real-time [1–3]. Diffuse reflectance spectroscopy has been extensively explored by us to measure tissue oxygenation [4,5], and it has been well-established by others as well to report hypoxia thereby predicting tumor therapeutic responses [2]. Autofluorescence spectroscopy has been explored by others [6] and us [7] to report the reduction-oxidation (redox) state of tissue by looking at the ratio of the two endogenous fluorophores (Flavin adenine dinucleotide (FAD), and reduced nicotine adenine dinucleotide (NADH)), and then provide an indirect measure of the balance between glycolysis and oxidative phosphorylation. To quantify tissue glycolysis and mitochondrial function directly and explicitly *in vivo*, we exploited several metabolic probes and integrated them with optical spectroscopy to report glucose uptake and mitochondrial function along with vascular parameters [4,5]. Our integration of diffuse reflectance and fluorescence

#502778
Journal © 2023
https://doi.org/10.1364/BOE.502778
Received 8 Aug 2023; revised 12 Sep 2023; accepted 16 Sep 2023; published 25 Sep 2023

spectroscopy with metabolic probes into one single device will provide rapid quantification of several key functional endpoints on the same tissue site at one time, which may potentially allow one to perform multi-dimensional metabolic analysis [8,9] on tumors that will provide more insights into cancer biology.

In most existing optical spectroscopy setups, a fiber probe consisting of single or multiple illumination and collection fibers was commonly used for light delivery and collection [10]. During the actual measurements, the fiber probe was usually placed above the tissue sample with gentle contact to minimize the specular reflectance. However, it has been reported that the inconsistent probe-sample contact could induce significant distortions in measured optical signals [11–13], which consequently would cause large data analysis errors. Moreover, it may be practically challenging to use a fiber probe for measurements in some cases such as oral cancer investigations where potential infection could be a concern or very early-stage tumor studies where the tumor is tiny to measure. To address these challenges, several groups reported non-contact optical spectroscopy setups for tissue characterizations. Adree et al. reported a lens-based spectroscopy setup to perform spatially resolved diffuse reflectance measurements on tissue samples [14]. In their platform, both illumination fiber and collection fiber were imaged onto the sample surface via a spherical mirror or achromatic lens to avoid fiber-sample contact. Bish et al. proposed a lens-based setup for non-contact diffuse reflectance measurements, while a fiber probe was still used and it was imaged onto the sample surface via an imaging lens [15]. Mazurenka et al. [16] reported a non-contact setup for time-resolved diffuse reflectance measurements in which laser scanning was used to achieve optical measurements without using a fiber probe. Non-contact fluorescence spectroscopy techniques have also been reported to achieve sensitive tissue characterizations. Mycek group reported a Monte Carlo method to simulate non-contact fluorescence from layered samples and validated their Monte Carlo technique using tissue-mimicking phantoms [17]. We reported a non-contact fluorescence device to achieve depth-sensitive imaging on layered phantoms [18].

As discussed above, most of the existing non-contact spectroscopy platforms primarily focused on diffuse reflectance measurements and may still use a fiber probe in which the probe was imaged onto the tissue surface using an imaging lens. Here we report a fiber-probe-free, dark-field based non-contact optical spectroscopy approach for both diffuse reflectance and fluorescence measurements on tissue samples. To optimize the system design, we developed a novel Monte Carlo technique to simulate such a non-contact setup for both diffuse reflectance and fluorescence measurements on murine subcutaneous tissue models with a spherical tumor-like target. We then performed Monte Carlo simulations on two unique subcutaneous tissue models including the small tumor models (with a tumor diameter of 6 mm at a depth of 1 mm) and the early-stage tumor models (with a tumor diameter of 3 mm at a depth of 0.2 mm) to identify the most tumor-sensitive configurations for most commonly used small tumor models. Our numerical studies showed that both the depth of the light focal point in tissue and the lens numerical aperture would dramatically affect the system's tumor detection sensitivity. In small tumor models, a larger depth of focal point always yielded an increased tumor detection sensitivity for both diffuse reflectance and fluorescence measurements but with a sacrifice of signal drops. For early-stage tumor models, a larger depth of light focal point yielded increased tumor detection sensitivity only for diffuse reflectance measurements but not for fluorescence measurements. In contrast, an optimal depth of light focal point exists for fluorescence measurements to provide the best tumor detection sensitivity for early-stage tumor models. For the two different tumor models, a smaller focal length of the lens (which has a larger numerical aperture) next to the sample always yielded better tumor detection sensitivity. We also found that the dark-filed technique can help fluorescence spectroscopy achieve increased tumor detection sensitivity compared to traditional white-field fluorescence spectroscopy. To solidify these findings, we developed a dark-field based non-contact optical spectroscopy and then conducted a series of tissue-mimicking phantom experiments.

Our phantom studies confirmed the key findings achieved from our numerical simulations. Our reported Monte Carlo technique can be a useful computational toolbox for designing non-contact optical spectroscopy systems. Our reported optical device and the corresponding findings will potentially offer a new approach for sensitive optical monitoring of tumor physiology in biological models using a non-contact optical spectroscopy platform to advance cancer research.

2. Materials and methods

2.1. *Monte Carlo method for dark-field non-contact optical measurements on layered tissue models with a spherical tumor-like target*

The schematics of our proposed lens-based non-contact setups for diffuse reflectance and fluorescence measurements are shown in Fig. 1(A) and (B), respectively. As shown in Fig. 1(A), a stopper and an iris were used to provide dark-field illumination and collection for diffuse reflectance measurements in which the specular reflectance can be effectively removed in actual measurements [19]. Figure 1(B) shows the schematics of the white-field non-contact fluorescence spectroscopy, while it should be noted that the dark-field technique can also be applied for fluorescence measurements. For Monte Carlo simulation studies, we assume that there was a point light source in Fig. 1(A) and (B), and this point light source will provide a collimated ring beam with the use of the condenser lens and the stopper. On the collection side, we assume the lens next to the collection fiber will be identical to the lens that was used next to the tissue sample so we can simplify the light collection procedure.

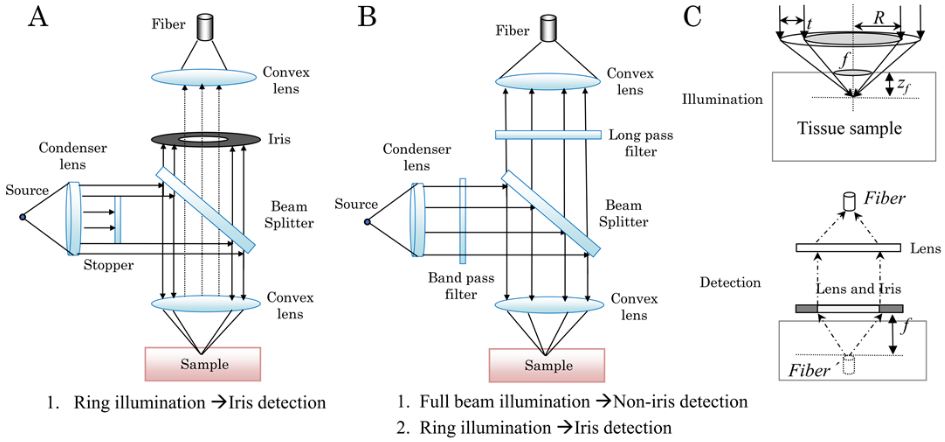
A
Fiber
Convex lens
Iris
Condenser lens
Source
Beam Splitter
Stopper
Convex lens
Sample
1. Ring illumination →Iris detection
B
Fiber
Convex lens
Long pass filter
Condenser lens
Source
Beam Splitter
Band pass filter
Convex lens
Sample
1. Full beam illumination →Non-iris detection
2. Ring illumination →Iris detection
C
t
R
f
z_f
Illumination
Tissue sample
Fiber
Lens
Detection
Lens and Iris
f
Fiber´

Fig. 1. (A) Schematics of dark-field based non-contact diffuse reflectance spectroscopy; (B) Schematics of lens-based non-contact fluorescence spectroscopy; (C) Monte Carlo schematic of dark-field illumination and collection.

Our formerly reported Monte Carlo method for the simulation of lens-based diffuse reflectance measurements on layered tissue models [20] was further developed to (1) simulate dark-field based fluorescence measurements in addition to diffuse reflectance measurements in the turbid medium; (2) simulate non-contact measurements on layered tissue models with a buried spherical tumor-like target. Figure 1(C) shows the Monte Carlo schematics of the potential focused illumination beam and lens-based light collection, and the major new procedures added to our formerly reported Monte Carlo method [20] are summarized below.

(1) Dark-field based illumination: The simulated illumination beam can be either a white-field full beam focused or a dark-field ring beam focused. Given the white-field focused beam illumination has been well described by others before [21], we only introduce the dark-field

based illumination here, which can be defined by the light beam diameter (R), the ring thickness (t), lens focal length (f), and the focal depth of light beam in tissue (z_f) as illustrated in Fig. 1(C) top. A Cartesian coordinate system was set up in the simulation to facilitate tracking the positions of photons. The initial light beam will be focused to form a ring on the tissue surface using the imaging lens. The illumination beam radius on the tissue surface can be calculated based on the relation that the ratio of the ring radius on the tissue surface to the ring radius on the lens (R) was identical to the ratio of the z_f to f, and the same method will be used to calculate the ring beam thickness on the tissue surface. The irradiance was assumed to be uniform on the tissue surface of the turbid medium and the radial position (r) of a photon packet will be randomly sampled by

$$r = \sqrt{[(\rho\_ring + t\_new)^2 - \rho\_ring^2] * \varepsilon + \rho\_ring^2} \tag{1}$$

where ρ_ring was the ring radius on the tissue surface, t_new was the ring thickness on the tissue surface, and ε was a random number uniformly distributed between 0 and 1. Once the radial position (r) was sampled, the Cartesian coordinates of the incident point were then

$$x = r * \cos(\theta), \tag{2}$$

$$y = r * \sin(\theta), \tag{3}$$

$$z = 0 \tag{4}$$

where the azimuthal angle $\theta = 2\pi * \varepsilon_\theta$, and the ε_θ was a random number uniformly distributed between 0 and 1. The directional cosines were then set to

$$ux = -x/\sqrt{r^2 + z^2} \tag{5}$$

$$uy = -y/\sqrt{r^2 + z^2} \tag{6}$$

$$uz = z_f/\sqrt{r^2 + z^2} \tag{7}$$

If the ambient medium and the tissue have different refractive index values, the directional cosines will be changed based on Snell's law, and the specular reflection was taken into account based on the Fresnel law when the photon entered the tissue. Once the photon was launched into the tissue model, the treatment of photon tracing for both diffuse reflectance and fluorescence was exactly as that done as reported previously [21–23].

(2) Dark-field based collection: A ray-tracing technique was used to simplify the detection of light from lenses and then the detection fiber [20] with the additional consideration of an iris, which is commonly used in dark-field techniques to remove the specular reflectance. To be brief, finding whether a photon is detected by a detection fiber is equivalent to identifying whether the photon can be traced back to its image inside the tissue (fiber′) due to the reciprocity of ray tracing as illustrated in Fig. 1(C) bottom. Once a photon exits the tissue surface, two steps will be performed to determine whether this photon can be detected by the detector. The first step is to determine whether this photon can pass through the iris, which can be done by moving the photon from the exit position to the plane of the iris along its exit direction. If the photon can pass through the iris, then the photon will continue to go through the second step, otherwise, the photon will not be detected and the detection procedure for this photon will be terminated. The second step is to perform ray retracing to determine if this photon could be detected by the detection fiber. This can be done by moving the photon from its exit position toward the plan of the imaging fiber along the opposite direction of its exit direction. Then both the fiber size and acceptance

angle (calculated from its numerical aperture value) will play a role in determining if the photon can be detected by the fiber. During the second step, the photon will be detected only if its exiting angle is smaller than the fiber acceptance angle and the photon can hit the fiber area, otherwise, the photon will not be detected. If a photon is detected by the fiber, all related trajectory information will be recorded for future data analysis.

(3) Non-contact measurements on layered tissue models with a finite tumor target: To more realistically mimic murine subcutaneous tumor models, a finite tumor model (Fig. 2(A)) consisting of a normal semi-infinite skin layer with a buried tumor-like spherical target was used [22]. The spherical target with a specified radius and position was used to mimic a solid tumor in murine subcutaneous tissues. The Monte Carlo code for simulating such tumor models was reported by us previously [22,24], but only for fiber-optics based diffuse reflectance and fluorescence measurement. Here, we have implemented this tumor model into our Monte Carlo code for dark-filed (and/or full beam) based non-contact diffuse reflectance and fluorescence measurements. To be brief, the spherical tumor's radius, depth location, and optical properties can be defined as needed. During each single photon move event, a tumor boundary detection procedure will be performed to determine if the photon is traveling to, traveling inside, or traveling out from the spherical tumor target. Then the photon weight, new step size, and new direction will be updated using the corresponding optical properties from tumor tissue or non-tumor tissue depending on its location. The details and validation of the Monte Carlo code for simulating such tumor models were published by us previously [22,24], though for fiber-probe based measurements only. The beam focal depth in the tumor models can be adjusted either via changing the lens-sample distance (d, Fig. 2(B)) or using a different lens with a different focal length for a fixed lens-sample distance (*f1, f2,* Fig. 2(C)).

(4) Simulation of diffuse reflectance and fluorescence using non-contact setups on layered tissue models with a finite tumor target: The simulation of lens-based diffuse reflectance measurements on layered tissue models has been well described by us before [20]. To be brief, the fluence rate distribution within the tissue volume and the updated photon weight are computed using the standard Monte Carlo method. Both the fluence rate and photon weight are governed by tissue absorption, scattering, refractive index, and the anisotropy factor. The final photon weight of detected photons will be used to calculate the diffuse reflectance. In contrast, the process for fluorescence simulation typically involves three primary steps. In the first step, the fluence rate distribution within the tissue volume is computed using the standard Monte Carlo method same as that done in the simulation of diffuse reflectance. In the second step, the spatial fluorescence distribution is determined by multiplying the fluence rate distribution by the intrinsic fluorescence profile. This intrinsic fluorescence profile is defined as the product of the fluorophore's absorption coefficient at the excitation wavelength and its quantum yield at the emission wavelength. Finally, the detected fluorescence is calculated as the convolution of the fluorescence source distribution throughout the tissue with Green's function. The intensity of the simulated local fluorescence is directly linked to the portion of absorbed energy, which is governed by the quantum yield of the fluorophore. Consequently, the distribution of the fluorescence source within the medium is primarily influenced by the distribution of the fluence rate [23,25]. Several Monte Carlo models were published for the simulation of fluorescence [23–28], while the Monte Carlo code for the simulation of fluorescence in this manuscript was modified from [23] which was originally based on [25]. Specifically, McShane et al. proposed the original concept of the fluorescence simulation [25], while Liu et al. further developed this fluorescence model with the use of fiber optics probes and validated the fluorescence model with homogenous phantoms [23]. Relying on these foundations, we

have further implemented the homogenous tissue model with a tumor-like target model to the existing fluorescence model but still used fiber-optics probes [22]. Relying on this most recent version, we further implemented the lens based dark-field technique to the existing fluorescence model [22] and then used the integrated approach to investigate the tumor-sensitive configurations for both diffuse reflectance and fluorescence measurements on subcutaneous tumor models. It should be noted that Monte Carlo techniques have been also developed to simulate fluorescence with more complicated conditions to facilitate different study requirements. For example, Vishwanath et al. reported a novel Monte Carlo model to simulate fluorescence lifetime in addition to fluorescence intensity and validated their method with phantom studies [27]. Churmakov et al. developed a novel Monte Carlo fluorescence model that takes into account the spatial distribution of fluorophores, the variation of concentrations and quantum yield in tissue models [28]. Swartling et al. reported novel Monte Carlo methods to accelerate the fluorescence simulation from layered tissue models [29].

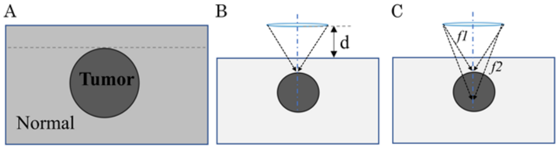

Fig. 2. (**A**) Finite tumor model to simulate small murine subcutaneous tumors; (**B**) Adjust focus depth via moving the sample towards or away lens; (**C**) Adjust optical focus depth via using different lenses with different focal lengths.

2.2. Tissue optical properties for both diffuse reflectance and fluorescence simulations

Two subcutaneous tissue models including the small tumor models (with a tumor diameter of 6 mm at a depth of 1 mm) and the very early-stage tumor models (with a tumor diameter of 3 mm at a depth of 0.2 mm) were used in our simulations to identify the most tumor-sensitive configurations for the non-contact spectroscopy (Fig. 1). The tissue optical properties used in our simulations were taken from previously published reports [5,30,31]. The detailed values of tissue optical properties are summarized in Table 1 [22]. Generally, tumor tissue has higher absorption, but lower reduced scattering coefficients compared to normal tissues. The wavelength of 550 nm was used for diffuse reflectance simulations as it is within the typical light band for oxygenation extraction and it is the excitation peak of our interested metabolic probe, i.e., Tetramethylrhodamine, ethyl ester (TMRE), to report mitochondrial function. For fluorescence simulations, the 550 nm light was used for excitation while the 585 nm light (TMRE emission peak) was used for emission. The quantum yields for tumor and normal tissue were set to be 0.5 and 0.3 respectively according to our previous studies [4,22].

Table 1. Optical properties of normal tissue and tumor [a]

Optical	Normal tissue				Tumor			
properties	μa (cm^{-1})	μs (cm^{-1})	g	n	μa (cm^{-1})	μs (cm^{-1})	g	n
550 nm	2.05	133.1	0.9	1.4	3.19	87.6	0.9	1.4
585 nm	1.36	122.2	0.9	1.4	2. 07	80.4	0.9	1.4

[a] From Biomed. Opt. Express 9, 3399-3412 (2018)

2.3. Simulation parameters for the lens and optical measurement configurations

To identify the tumor-sensitive configurations of the non-contact spectroscopy for diffuse reflectance and fluorescence measurements, Monte Carlo simulations were performed on the finite tumor models described in Fig. 2. To ensure the fluorescence excitation light was always delivered to the central mass of the tumor, the center of the illumination lens always overlapped with the vertical middle line of a spherical tumor as shown in Fig. 2(B)-(C). The refractive index of the ambient medium between the lens and the tissue sample was set to 1.0 which represented the refractive index of air. The numerical aperture value of the detection fiber was set to 0.22 and the diameter of the detection fiber was set to 0.4 mm. The lens diameter was set to 25.4 mm, which was the typical size for commercially available lenses. The other parameters investigated in the simulations for the dark-field ring beam or white-field full beam, depth of light beam focus, and lens focal lengths are listed in Table 2. Ten million photons were used in each independent simulation, which was repeated four times to estimate the means and standard deviations for the construction of error bars shown in the results section.

Table 2. Simulated configurations for the non-contact spectroscopy[a]

Parameters	Values under investigation
Depth of focal point in tissue (mm)	0.2, 0.5, 1.5, 3.0, 4.0, 5.0
Lens focal length (mm)	20, 30, 40, 50
Ring beam diameter (mm)	8.0, 6.0
Stopper and iris diameter (mm)	6.0, 4.0

[a] The lens focal depth values were selected based on the commonly seen lens, while the depth of the focal point in tissue was selected based on the tumor depth in two different tumor models. For dark-field simulations, the stopper and iris diameter were 6.0 mm when the ring beam diameter was 8.0 mm, while the stopper and iris diameter were 4.0 mm when the ring beam diameter was 6.0 mm. For full beam simulations, neither a stopper nor an iris was used.

2.4. Experimental setup and tissue-mimicking phantoms

To solidify the key findings obtained from our simulations, we also developed a compact dark field-based non-contact optical spectroscopy using the schematic shown in Fig. 3(A). A Solis white LED (SOLIS-3C, Thorlabs) and a compact visible spectrometer (FLAME-T-VIS-NIR, Ocean Optics) were used to build the spectroscopy platform. In the illumination end, a fiber with a diameter of 1.5 mm (M93L01, Thorlabs) and one condenser lens with a focal length of 25.4 mm (LB1761, Thorlabs) were used to generate an illumination beam with a diameter of around 8 mm. A 3D printed stop with a diameter of 6 mm was used in front of the beam splitter to generate ring illumination beams as needed, while an iris (4 mm in diameter) was used next to the beam splitter for collection during diffuse reflectance measurements but not for fluorescence measurements. At the collection end, a convex lens with a focal length of 25.4 mm (LB1761, Thorlabs) and a round to linear fiber (BFL200LS02, Thorlabs) was used to collect as much signal as possible. A bandpass (540 nm) filter and a long pass filter (580 nm cutoff) were installed in the filter wheels to facilitate fluorescence measurements, while no filter was used for diffuse reflectance measurements. The optical sample stage would allow changing the light focal depth by adjusting the distance between the sample and the imaging lens for a given lens. The imaging lens between the sample stage and the beam splitter can also be easily replaced if a lens with a different focal length is used. In our system design, we wanted to minimize the distance between the imaging lens and the stop (which was mounted on the right side of the beam splitter) to ensure: 1) the ring beam that enters the imaging lens will be the same for different imaging lens with a different focal length; 2) minimize the system size for future on-site experiments; 3) reduce the system complexity for actual experiments. The potential impact of this choice is that the focal spot size in the tissue might be different from one imaging lens to another, which may potentially affect the performance of the system for tumor measurements. Figure 3(B) shows the actual compact dark-field based non-contact optical spectroscopy with optical components arrangement information for both diffuse reflectance and fluorescence measurements on tissue-mimicking phantoms.

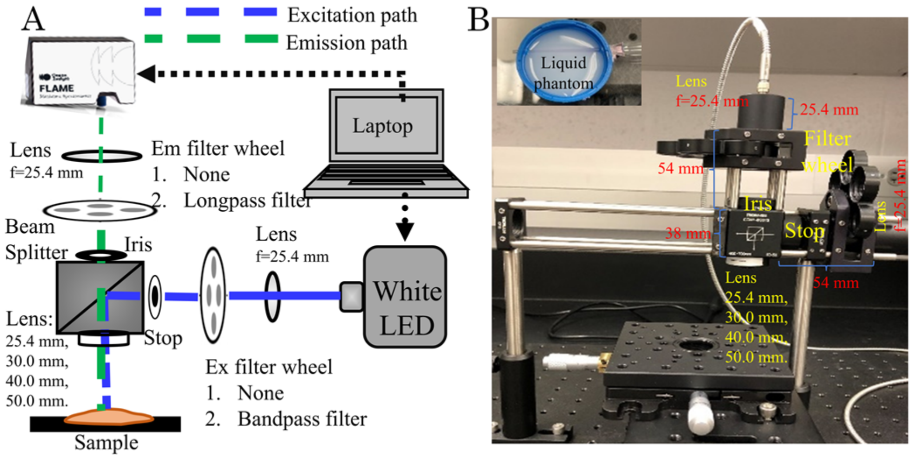

Fig. 3. (**A**) Dark-field based non-contact optical spectroscopy schematic; (**B**) Compact dark-field based non-contact optical spectroscopy for tissue-mimicking phantom studies and liquid tissue-mimicking phantom.

To test the system for tumor-sensitive diffuse reflectance measurements on turbid medium with a tumor-like target, liquid phantoms with a buried cylindrical tumor-like target (Fig. 3(B) top left) were created using India ink and Intralipid (Sigma-Aldrich). The reduced scattering coefficient of the phantoms was 10 cm^{-1} on average for 400 nm -600 nm, while the absorption coefficient of the liquid phantoms was set to zero. One glass tube (~1 mm inner diameter with a wall thickness of 0.3 mm) was buried in the liquid phantoms with a depth of 1.0 mm to mimic the tumor-like target. India ink liquid was injected into the glass tube to mimic the high absorption of tumors. It should be noted that this simple phantom with a tumor-like target here may not accurately represent the genuine tumor absorption characteristics but will be sufficient to allow us to validate the key simulation findings for a proof-of-concept study. To further test the system for diffuse reflectance measurements on tissue-like samples, both homogeneous tissue-mimicking phantoms and volunteer finger tissues were measured. The optical properties of the phantoms were designed based on the formerly reported optical properties of mice skin [32]. Specifically, the homogeneous phantoms had the following average absorption coefficients and reduced scattering coefficients (400-600 nm): μ_a= [1.5, 3.0, 4.5] cm^{-1} and μ'_s = [5,10] cm^{-1}. Dehydrated human hemoglobin powder (H0267, Sigma-Aldrich) was used as a major absorber in the phantoms (concentration varies from 0.92 mg/ml to 2.76 mg/ml to have the above absorption coefficients). 20% intralipid (Sigma-Aldrich) was used to mimic tissue scattering (concentration varies from 0.312% to 0.624%). Phosphate Buffered Saline (PBS) 1x (Fisher Scientific) was used to suspend the intralipid and hemoglobin for the liquid phantoms. To test the system for tumor-sensitive fluorescence measurements, similar phantoms with a buried tumor-like target were created. The absorption and scattering properties of the phantoms were the same as those used for diffuse reflectance measurements but with an addition of fluorophore. TMRE solutions were injected into the glass tube to mimic the increased TMRE uptake in tumors compared to normal tissue. The concentration ratio of tumor to the non-tumor regions was set to 5/3

(500 nM /300 nM) to highlight their different TMRE uptakes. For either diffuse reflectance or fluorescence tumor-like target contrasts or intensities change investigations, all the optical measurement configurations including the integration time, depth of light beam focus, lens focal length, and others were kept exactly the same for both finite tumor phantom measurements and non-tumor control phantom measurements.

2.5. Data analysis

The Monte Carlo simulated diffuse reflectance and fluorescence intensities were used to represent the collected optical signals for data analysis. The tumor contrasts for both diffuse reflectance and fluorescence introduced by us previously [22] were used to evaluate the optical detection sensitivity of the tumors. Specifically, the tumor contrast for diffuse reflectance was defined as the percent deviation of weighted photon visiting frequency (WVF) [33] in the tumor region to that from the entire tissue region. The WVF refers to the number of times that photons visit a region divided by the total attenuation coefficient at a given region [33]. The tumor contrast of reflectance (TC_R) was calculated based on Eq. (1).

$$TC_R = \frac{WVF_{tumor}}{WVF_{tumor} + WVF_{normal}} \tag{8}$$

The WVF_{tumor} referred to the weighted photon visiting frequency in the tumor region, while the WVF_{normal} referred to the weighted photon visiting frequency in the normal tissue region. The tumor contrast for fluorescence (TC_F) was calculated as the percent deviation for detected fluorescence generated from the tumor region to the total detected fluorescence from the entire tissue model, which was calculated based on Eq. (2).

$$TC_F = \frac{F_{tumor}}{F_{tumor} + F_{normal}} \tag{9}$$

The F_{tumor} referred to the fiber-detected fluorescence signal contributed by the tumor region, while the F_{normal} referred to the fiber-detected fluorescence contributed by the normal tissue. Generally, a higher tumor contrast refers to a higher tumor detection sensitivity. The interrogation depth [34] was used to further quantify the optical tumor sense capabilities [35]. The diffuse reflectance interrogation depth was obtained by examining the WVF distribution along the Z-axis direction [33], and the fluorescence interrogation depth was acquired by examining the function of surface-measured fluorescence with the occurring position along the Z-axis [23]. The experimentally obtained diffuse reflectance and fluorescence spectra were used to characterize the changes for either tumor contrasts or optical intensities for different optical configurations. The phantom tumor contrasts for diffuse reflectance and fluorescence were defined as the percentage ratios of optical signal changes caused by the presence of a tumor-like target. The signal changes were calculated based on optical spectra measured on the phantoms with a tumor-like target and on the phantoms without a tumor-like target (serves as control). The phantom tumor contrasts ($TC_{phantom}$) were calculated using Eq. (3).

$$TC_{phantom} = \frac{|I_{tumor} - I_{control}|}{I_{control}} \tag{10}$$

where I_{tumor} referred to either fluorescence or diffuse reflectance intensities measured on the phantoms with a tumor-like target, while $I_{control}$ referred to optical intensities (fluorescence or diffuse reflectance) measured on the control phantoms that do not have a tumor-like target. Diffuse reflectance intensities at 540-560 nm and fluorescence intensities at 580-600 nm were used to calculate the tumor contrasts.

3. Results

3.1. *Effect of the focal depth of light beam in tissue and beam size on optical intensity and tumor contrast for darkfield-based diffuse reflectance measurements*

Figure 4 showed WVF distributions along the Z-axis, tumor contrasts, and intensities for dark field diffuse reflectance measurements for the early-stage tumor models and small tumor models, respectively. The WVF distributions could inform the optical interrogation depth that indicates the optical sensing depth [35], and they could also support the tumor contrast changes where an increased tumor contrast was reflected by an increased WVF in the tumor region and a decreased WVF in the non-tumor region. For both tumor models, the WVF distributions showed that the optical interrogation depth was increased when the light beam focal depth was increased. The diffuse optical interrogation depth for early-stage tumors can reach up to ∼2 mm when the light beam focal depth is equal to or larger than 3.0 mm as evidenced by the considerable WVF in the depth range of ∼2 mm shown in Fig. 4(A) and (B). However, the interrogation depth for small tumor models was ∼1.5 mm as shown in Fig. 4(E) and (F). Figures 4(C) and (G) showed that the tumor contrast from diffuse reflectance was increased significantly when the light beam focal depth was increased from 0.2 mm to 5 mm but with significant signal drops as shown in Fig. 4(D) and (H) for both two tumor models. Generally, a larger ring beam size yielded increased tumor contrasts. Consequently, a larger ring beam size led to decreased optical signals compared to a smaller ring beam size.

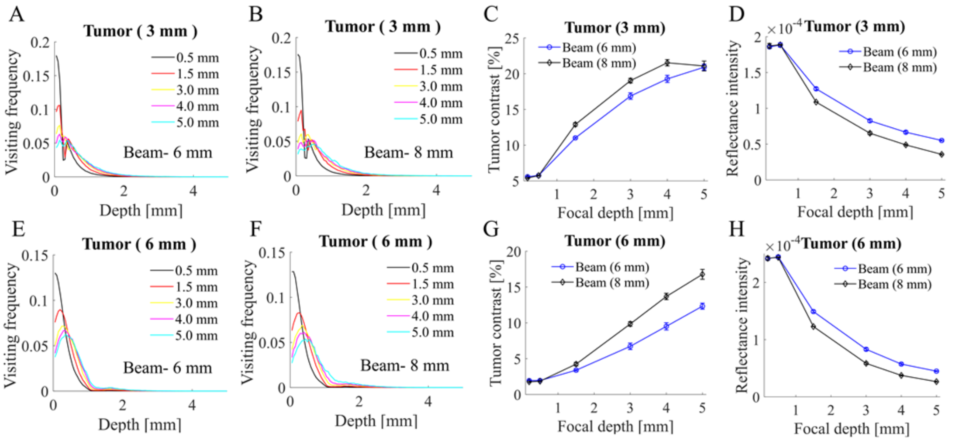

Fig. 4. WVF for dark field diffuse reflectance measurements on early-stage tumor models with a beam size of 6 mm (**A**) and 8 mm (**B**); Tumor contrasts (**C**) and diffuse reflectance intensities (**D**) for simulations conducted on early-stage tumor models; WVF for dark field diffuse reflectance measurements on small tumor models with a beam size of 6 mm (**E**) and 8 mm (**F**); Tumor contrasts (**G**) and diffuse reflectance intensities (**H**) for simulations conducted on small tumor models. The lens focal length was 20 mm. The stop size was 4 mm and 6 mm, respectively, when the beam size was 6 mm and 8 mm to generate ring illumination beams. The iris size was the same as the stop size.

3.2. *Effect of the lens numerical aperture on optical intensity and tumor probing sensitivity for dark field-based diffuse reflectance measurements*

Figure 5 showed tumor contrasts, reflectance intensities, and the representative WVF distributions along the Z-axis direction for dark field diffuse reflectance measurements using four lenses with different focal lengths (which lead to different numerical apertures) for both the early-stage tumor models and small tumor models. Figures 5(A) and (D) showed that the optical tumor detection sensitivity was increased significantly for all four lenses when the light beam focal depth was increased from 0.2 mm to 5 mm, while the lens with a shorter focal length (with a larger numerical aperture) always yielded better tumor contrasts. Figures 5(B) and (E) showed that the diffuse reflectance intensities decreased significantly for all four lenses when the light beam focal depth was increased from 0.2 mm to 5 mm. However, the optical signals were generally increased first and then decreased when the lens focal length was increased from 20 mm to 50 mm. Figures 5(C) and (F) showed the representative WVF distributions along the Z-axis direction for all four different lenses at a fixed light beam focal depth of 4 mm. A decreased WVF in the non-tumor region and an increased WVF in the tumor region for the lens with a shorter focal length as shown in Fig. 5(C)- (F) explained their increased tumor contrasts shown in Fig. 5(A) and (D).

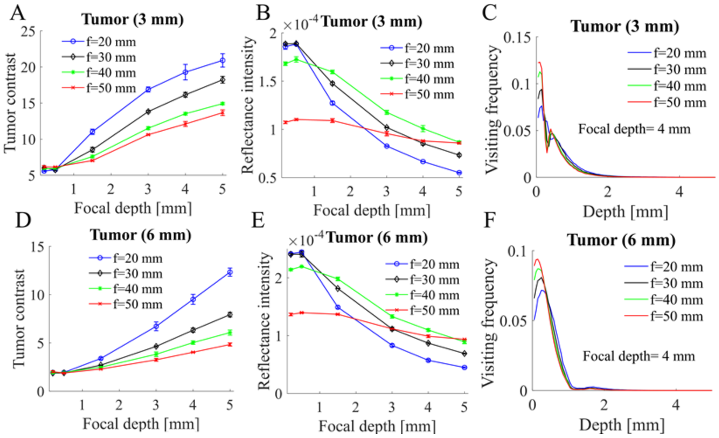

Fig. 5. Tumor contrasts (**A**), diffuse reflectance intensities (**B**), and the representative WVF distributions (**C**) for simulations using four lenses with different focal lengths on early-stage tumor models; Tumor contrasts (**D**), diffuse reflectance intensities (**E**), and the representative WVF distributions for simulations using four lenses with different focal lengths on small tumor models (**F**). The beam size was set to be 6 mm and the stop size was set to be 4 mm to generate the ring illumination beams. The iris size was the same as the stop size.

3.3. Experimental validations for non-contact diffuse reflectance measurements

Figure 6(A) shows the representative diffuse reflectance spectra measured on liquid phantoms with a tumor-like target using an imaging lens with a focal length of 25.4 mm. As expected, diffuse reflectance intensities decreased when the depth of the light focal point was changed from 0 (tissue surface) to 4.5 mm (below the cylindrical target). Figure 6(B) shows the tumor contrasts for diffuse reflectance measurements using four lenses with different focal lengths on the liquid phantoms. The tumor contrast changes showed that the tumor detection sensitivity was increased significantly for the lens with a focal length of 25.4 mm when the light beam focal depth was increased from 0 mm to 4.5 mm, while there were minimal increases in tumor contrasts for the other three lenses. Generally, the lens with a shorter focal length has a better tumor detection sensitivity compared to the lens with a longer focal length, which is consistent with the simulation results shown in Fig. 5. Figure 6(C) shows the reflectance spectra measured on six homogeneous phantoms with optical properties covering both normal and tumorous tissues in mice subcutaneous tumor models [36]. As expected, the diffuse reflectance decreased with increased absorption levels when the reduced scattering level was fixed for both high-scattering and low-scattering phantoms, while the diffuse reflectance intensities at the scattering domain (650-700 nm) were proportional to the reduced scattering levels when the absorption level is fixed.

Figure 6(D) shows the corresponding diffuse reflectance spectra measured in one volunteer's fingertip, backside of finger, and fingernail site. The spectra showed that our system captured that the tissues in three regions of one finger had different absorption levels (absorption band in 530-580 nm) and scattering levels (600-700 nm band) as expected. These spectra had significantly different shapes, which suggested that these tissues have significantly different optical properties. The spectral shapes in Fig. 6(C) and (D) demonstrated the feasibility of our non-contact diffuse reflectance spectroscopy for future quantitative characterization of tissue vascular parameters.

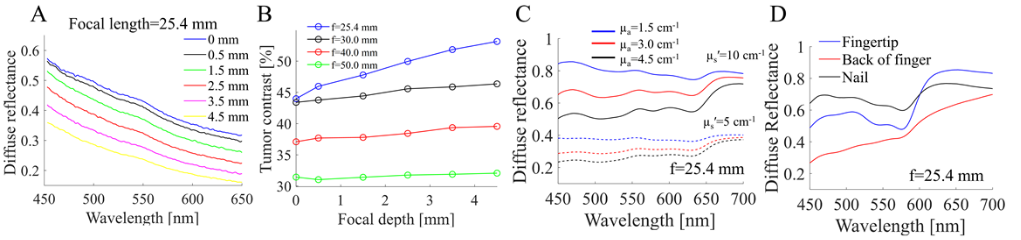

Fig. 6. (**A**) Representative diffuse reflectance spectra measured on liquid phantoms with a tumor-like target. The focal length of the lens next to the sample was 25.4 mm. The depth of the light focal point was changed from zero (surface) to 4.5 mm. (**B**) Tumor contrasts for different lenses (biconvex from Thorlabs) used next to the sample. The focal lengths of the lenses were 25.4 mm, 30.0 mm, 40.0 mm, and 50.0 mm. (**C**) Diffuse reflectance spectra measured on tissue-mimicking phantoms with optical properties covering both normal and tumor tissues. (**D**) Diffuse reflectance spectra measured on one volunteer's finger tissues. The beam size was ~ 8 mm, and the stop size was set to 6 mm to generate the ring illumination beams. The iris size was set to 4 mm. The integration time for measurements was 25 ms.

3.4. *Effect of the focal depth of light beam in tissue and beam size on optical intensity and tumor probing sensitivity for non-contact fluorescence measurements*

Figure 7 shows the simulation results for white-field full beam (two different beam sizes) focused fluorescence measurements with different light beam focal depths on two different tumor models. Similar to WVF in diffuse reflectance, the fluorescence frequency distributions could inform the fluorescence occurring depths and support the fluorescence tumor contrast changes where an increased tumor contrast originated from an increased fluorescence frequency in the tumor region but a decreased fluorescence frequency in the non-tumor region.

For both two tumor models, the fluorescence signals contributed from non-tumor regions were decreased when the focal depth was increased from 0.2 mm to 5 mm as shown in Fig. 7(A)-(B) and Fig. 7(E)-(F). In contrast, the fluorescence signals originating from tumor regions were generally increased when the focal depth was increased. The fluorescence signals-based tumor contrasts in Fig. 7(C) showed that the fluorescence detection sensitivity of early-stage tumors was increased significantly when the light beam focal depth was increased from 0.2 mm to 3.0 mm, and then slightly decreased when the light beam focal depth was increased from 3.0 mm to 5.0 mm. However, Fig. 7(G) showed that the fluorescence detection sensitivity of small tumors was continuously increased when the light focal depth was increased from 0.2 mm to 5.0 mm. Figures 7(D) and (H) showed that the fluorescence intensities decreased significantly when the light beam focal depth was increased from 0.2 mm to 5 mm for both the two tumor models. Generally, a larger illumination beam size yielded slightly increased tumor contrasts but slightly decreased optical signals. The increased tumor contrast shown in Figs. 7(C) and (G) was reflected by an increased fluorescence frequency in the tumor region and decreased fluorescence frequency in the non-tumor region.

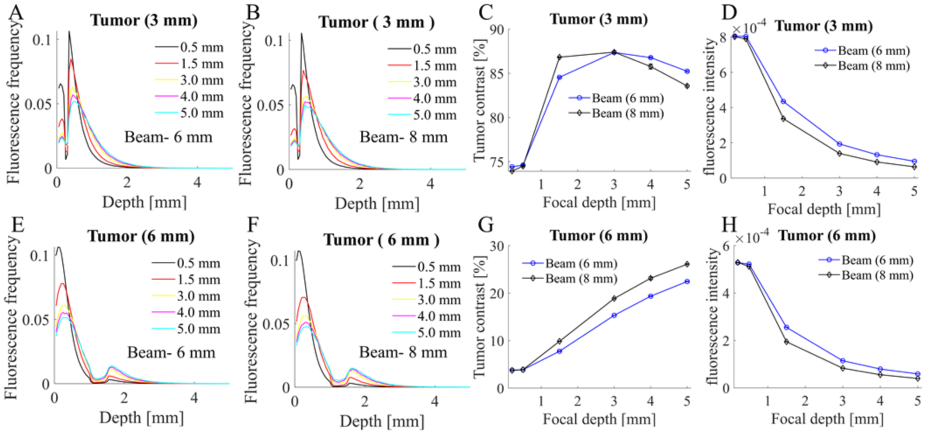

Fig. 7. Fluorescence frequency on early-stage tumor models with a beam size of 6 mm (**A**) and 8 mm (**B**); Tumor contrasts (**C**) and fluorescence intensities (**D**) for simulations conducted on early-stage tumor models; Fluorescence frequency for fluorescence measurements on small tumor models with a beam size of 6 mm (**E**) and 8 mm (**F**); Tumor contrasts (**G**) and fluorescence intensities (**H**) for simulations conducted on early-stage tumor models. White-field full beam focused illumination was used in all simulations, which was commonly used in existing non-contact fluorescence spectroscopy. The lens focal length was fixed to be 20 mm. Neither a stop nor an iris was used.

3.5. Effect of different illumination and collection configurations on optical intensity and tumor probing sensitivity for non-contact fluorescence measurements

Figure 8 shows the comparisons between the white-field full beam focused and dark-field ring beam focused non-contact fluorescence measurements on the two different tumor models. For both two tumor models and two different optical configurations, the fluorescence signals contributed from tumor regions were generally increased when the focal depth was increased, while the fluorescence contributed from non-tumor regions were decreased consequently as shown in Fig. 8(A)-(B) and Fig. 8(E)-(F). Figure 8(C) showed that the tumor contrasts for the early-stage tumor models were increased significantly first and then decreased slightly when the focal depth was increased from 0.2 mm to 5.0 mm for both the two different optical configurations. However, the dark-field approach yielded the highest tumor contrast when the light beam was focused inside the tumor region. Figure 8(G) showed that the tumor contrasts for the small tumor models were always increased when the focal depth was increased for both the two different optical configurations, while the dark-field approach always yielded increased tumor contrast compared to the while-field approach at all different focal depths. Figures 8(D) and (H) showed that the fluorescence intensities decreased significantly when the light focal depth was increased from 0.2 mm to 5 mm for both the two tumor models and the two optical configurations. Generally, the dark-field technique yielded decreased fluorescence intensities compared to the traditionally used white-field approach.

3.6. Effect of the lens numerical aperture on optical intensity and tumor probing sensitivity and for non-contact fluorescence measurements

Figure 9 shows the performances of dark field-based fluorescence measurements using four lenses with different focal lengths (which lead to different numerical apertures) for both the early-stage tumor models and small tumor models. Figure 9(A) showed that the fluorescence tumor contrast for early-stage tumors was increased significantly first and then decreased for all four different

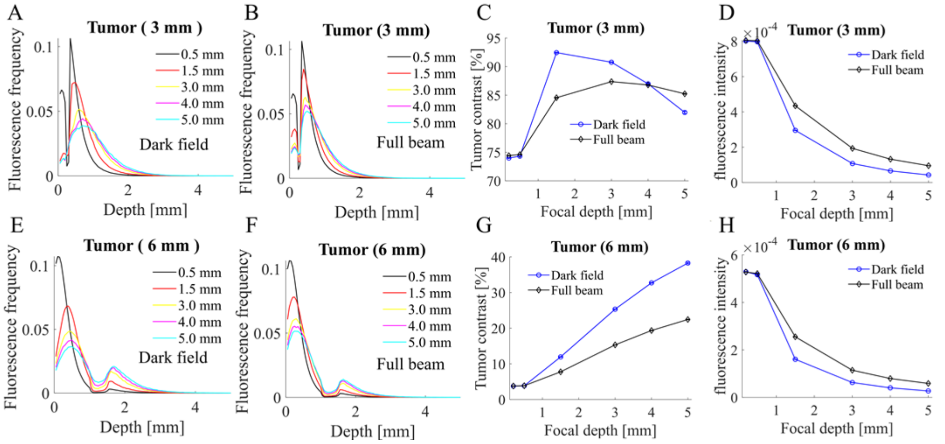

Fig. 8. Fluorescence frequency with dark-field beam focused illumination (**A**) and white-field full beam focused illumination (**B**) on early-stage tumor models; Tumor contrasts (**C**) and fluorescence intensities (**D**) for simulations using dark-field approach and white-field approach conducted on early-stage tumor models; Fluorescence frequency with dark-field beam focused illumination (**E**) and white-field full beam focused illumination (**F**) on small tumor models; Tumor contrasts (**G**) and fluorescence intensities (**H**) for simulations using dark-field approach and white-field approach conducted on small tumor models. The lens focal length was fixed to be 20 mm. The beam size was fixed to be 6 mm. In dark-field simulations, the stopper size was set to be 4 mm to generate the ring illumination beams, the iris was set to be 4 mm. In white-field simulations, neither a stop nor an iris was used.

lenses when the light beam focal depth was increased from 0.2 mm to 5.0 mm. An optimal focal depth of light beam exists for fluorescence measurements for all different lenses to provide the best tumor detection sensitivity for the early-stage tumor models. Differently, Fig. 9(D) showed the fluorescence detection sensitivity of small tumors was increased continuously for all four lenses when the light beam focal depth was increased from 0.2 mm to 5.0 mm. For both the two tumor models, the lens with a shorter focal length (which has a larger numerical aperture) had better performance in terms of the tumor contrasts. Figures 9(B) and (E) showed that the fluorescence intensities decreased significantly when the light beam focal depth was increased from 0.2 mm to 5 mm for all four different lenses in both early-stage tumor models and small tumor models. However, the optical signals were generally increased when the lens focal length was increased from 20 mm to 50 mm for a fixed light beam focal depth. Figures 9(C) and (F) showed the fluorescence frequency distributions for all four different lenses at a fixed light beam focal depth of 4 mm, which may explain their corresponding tumor contrasts and fluorescence intensity changes.

3.7. Experimental validations for non-contact fluorescence measurements

Figure 10(A) shows the representative fluorescence spectra measured on liquid phantoms with a tumor-like target using an imaging lens with a focal length of 25.4 mm. As expected, fluorescence intensities increased first and then decreased when the depth of the light focal point was changed from 0 (tissue surface above the target) to 4.0 mm (below the target). Figure 10(B) shows the tumor contrasts for fluorescence measurements using four lenses with different focal lengths on the liquid phantoms. The tumor contrasts were increased when the light beam focal depth was increased from 0 mm to 4.5 mm for all four lenses, while the lens with a shorter focal length had a higher tumor contrast compared to the lens with a longer focal length. Figure. 10(C) shows dark field based fluorescence measurements provided increased tumor contrasts compared to

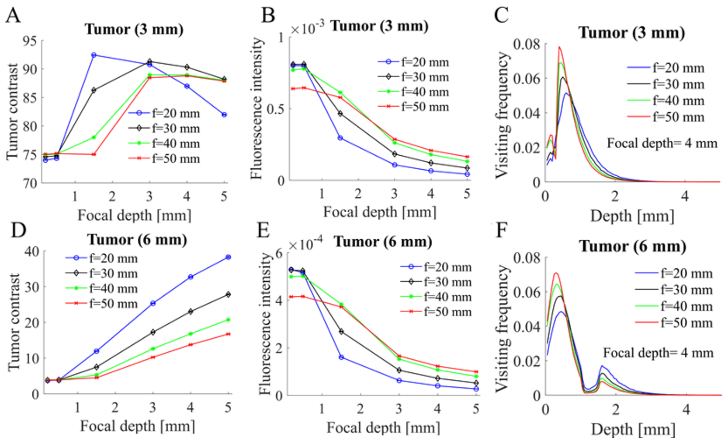

Fig. 9. Tumor contrasts (**A**), fluorescence intensities (**B**), and the representative fluorescence frequency distributions (**C**) for simulations using four lenses with different focal lengths on early-stage tumor models; Tumor contrasts (**D**), fluorescence intensities (**E**), and the representative fluorescence frequency distributions for simulations using four lenses with different focal lengths on small tumor models (**F**). The beam size was set to be 6 mm and the stop size was set to be 4 mm to generate the ring illumination beams. The iris size was the same as the stop size.

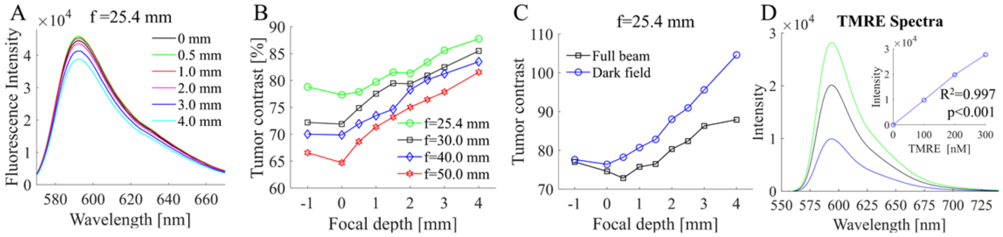

Fig. 10. (**A**) Representative fluorescence spectra measured on liquid phantoms with a tumor-like target. The focal length of the lens next to the sample was 25.4 mm. The depth of the light focal point was changed from zero to 4.0 mm. (**B**) Tumor contrasts using full-beam illumination based fluorescence measurements for different lenses (biconvex from Thorlabs) used next to the sample. The focal lengths of the lenses were 25.4 mm, 30 mm, 40 mm, and 50 mm. (**C**) Dark-field illumination based fluorescence measurements provided better tumor detection sensitivity compared to the full beam illumination based fluorescence measurements. The beam size was ~ 8 mm, and the stop size was set to 6 mm to generate the ring illumination beams. No iris was used for fluorescence measurements. (**D**) Fluorescence spectra were measured on liquid phantoms (10 cm^{-1} scattering) with probes at biologically low concentrations. The integration time for all measurements was 50 ms.

full beam illumination based fluorescence measurements, it is also interesting to see that the tumor contrasts increased faster using dark field compared to full beam illumination when the focal point was increased from the tissue surface to a deeper region. The experimental results in Fig. 10(B)-(C) are generally consistent with the simulation results shown in Fig. 9. Figure. 10(D) shows the fluorescence spectra measured on liquid phantoms that reflect the sensitivity of the optical device for quantifying the metabolic probe at biologically low concentrations. A linear correlation between the peak fluorescence intensity and fluorophore concentration was observed for the metabolic probe as expected ($R^2 = 0.997$, and $p < 0.001$). The fluorescence data measured on liquid phantoms with low concentrations demonstrated the feasibility of our non-contact spectroscopy for future sensitive characterization of metabolic parameters.

4. Discussion

Diffuse reflectance spectroscopy has been well established to quantify tissue vascular parameters [2], while fluorescence spectroscopy has been explored extensively to report cell metabolism [4,5]. The combination of diffuse reflectance and fluorescence spectroscopy enables simultaneous measurements of several key functional parameters on the same tissue site, which potentially allows multi-dimensional metabolic analysis [8,9] of tumors that will provide more insights into cancer biology. Fiber probes are commonly used in biomedical spectroscopy platforms for optical measurements. However, the use of fiber probes in optical spectroscopy platforms could bring several practical problems including significant analysis errors due to the inconsistent probe sample contact and infection concerns. Moreover, it may be practically challenging to design a proper probe for some cases such as oral cancer studies or very early-stage tumor investigations [22]. To address these challenges, we first reported a novel Monte Carlo method to simulate dark-field non-contact spectroscopy for both diffuse reflectance and fluorescence measurements on murine subcutaneous tissue models with a spherical tumor-like target. We then conducted numerical studies to identify the most tumor-sensitive configurations for such a non-contact spectroscopy device. Relying on these findings, we developed and demonstrated a compact non-contact spectroscopy platform to perform tumor-sensitive diffuse reflectance and fluorescence measurements on tissue-mimicking phantoms.

Our simulations of dark field non-contact diffuse reflectance on two unique subcutaneous tumor models showed that the illumination beam focal depth significantly affected the tumor detection sensitivity. Our data showed that the tumor contrast was increased when the focal depth was increased for both tumor models, which can be explained by diffusion theory. A larger depth of the illumination beam focus would lead to a deeper sensing depth where the tumor was located, which will monotonically increase the tumor contrast. The diffuse reflectance intensities dropped significantly when the focal depth was increased, which is likely because of the two following reasons: 1) the collected photons will be attenuated more when they travel deeper; 2) the increased contribution from tumor tissue attenuation could further lead to lower diffuse reflectance intensities because of higher absorption and lower scattering of tumors used in our simulations. We also found that the imaging lens with a shorter focal length always yielded better tumor contrasts compared to the imaging lens with a longer focal length, which may be explained by the numerical apertures of the illumination and collection beams. The imaging lens with a shorter focal length had a larger numerical aperture compared to the lens with a longer focal length. From the illumination perspective, a larger numerical aperture of a lens would allow to form a smaller focal spot inside the tissue which will potentially allow more photons to interact with the focal region, i.e., tumor target in this study. From the collection perspective, a larger numerical aperture of a lens would provide a larger accept angle of the lens which will potentially allow the system to collect more photons from the focal plane inside the tissue (i.e., tumor target in this study). Altogether, the imaging lens with a shorter focal length would provide increased tumor contrasts compared to the lens with a longer focal length because of its larger numerical aperture. This numerical aperture explanation is further supported by the findings that the larger illumination beam (8 mm) provided better tumor contrasts compared to the smaller illumination (6 mm) for a given lens as shown in Fig. 5(C) and (G).

Our simulations of non-contact fluorescence measurements showed that the fluorescence tumor contrasts changes in terms of light beam focal depth are different for the two unique subcutaneous tumor models. Specifically, the fluorescence tumor contrasts for early-stage tumor models (tumor diameter is 3 mm and depth is 0.2 mm) had a turning point that had the best tumor detection sensitivity when the light beam focal depth was increased from 0.2 mm to 5 mm. The phenomenon for early-stage tumor models could be explained by the fact that the tiny tumor was in a very shallow region, a deeper light beam focal depth may potentially cause more excitation lights to be delivered into the non-tumor tissue region. Different from diffuse reflectance, the fluorescence was isotropic thus the configuration of using a deeper light beam focal depth may also cause less fluorescence from the tumor region to be detected. In contrast, the fluorescence tumor contrast for small tumor models (tumor diameter is 6 mm and depth is 1 mm) was continuously increased when the light beam focal depth was increased. The findings for small tumor models could be explained by the fact that the small tumor was in a relatively deeper region thus the diffuse theory played a significant role in the excitation light delivery, where a larger light focal depth could allow more excitation lights to be delivered to the tumor region. Nevertheless, these results suggested that the thumb role for choosing the light beam focal depth for non-contact spectroscopy measurements should be treated differently for different tumor models, which can be easily obtained from Monte Carlo simulations. It is interesting to see that the fluorescence frequency increased first and then decreased around the tumor region for both two models as shown in Figs. 7(A) and (E). The small bump, which was close to the tumor boundary, is likely because there was an increase first in fluorescence due to the tumors having a higher fluorescence quantum yield compared to normal tissues. However, the fluorescence around this region will start to drop with the depth due to the scattering effect on the collected fluorescence. Similar to that seen in diffuse reflectance simulations, the imaging lens with a shorter focal length always yielded better performance in our fluorescence simulations, and the larger illumination beam provided better tumor contrasts, both can be explained by the numerical apertures theory as discussed above. We are also interested in maximizing the fluorescence tumor detection sensitivity, thereby we compared the white-field and dark-field techniques for non-contact fluorescence measurements on the two different tumor models. Our results showed that the dark-field technique provided significantly improved tumor detection sensitivities compared to the white-field approach. This is likely because the dark-field technique could minimize the chances for the excitation light to be delivered to the non-tumor region above the tumors. However, it should be noted that the dark-field technique has one potential drawback as the use of stop could block a significant excitation power from the light source. A tradeoff needs to be made when one chooses to use the dark-field technique or full-beam approach for fluorescence measurements. If the full-beam based fluorescence spectroscopy cannot provide sufficient tumor detection sensitivity for relatively deeper tumor sensing, one may want to employ the dark-field technique to increase the depth sensitivity of the system but with special consideration in using a high-power illumination light source. Otherwise, the use of the full-beam approach may be sufficient to provide tumor-sensitive measurements for certain applications such as superficial tumor detection.

For early-stage tumor models, we noticed that both diffuse reflectance-based contrast and fluorescence-based contrast reached a plateau when the focal depth was increased from the surface to the depth just below the tumor target as seen in Fig. 4(C) and Fig. 7(C), respectively. This interesting phenomenon is likely because the photons reached the tumor boundary when the focal depth was set just below the tumor for early-stage tumor models. When the photons were focused below the tumor boundary area, the photons that would interact with the tumor target will not significantly increase or may potentially decrease which will lead to unchanged or decreased tumor detection contrasts. To further test this hypothesis, we run additional simulations for the small tumor model (diameter is 6 mm) with more focal depths that reach to tumor boundary. The simulation results confirmed this hypothesis as shown in Fig. 11. Figure 11(A) showed that the diffuse reflectance-based tumor contrast reached a plateau (for the illumination beam of 6 mm) or decreased (for the illumination beam of 8 mm) when the depth focal was increased from the surface to the tumor boundary. Figure 11(B) showed that the fluorescence-based tumor contrast reached a plateau for both the illumination beam sizes when the depth focal was increased from the surface to the tumor boundary.

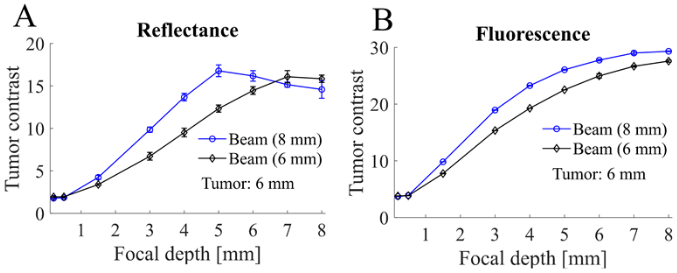

Fig. 11. (**A**) Diffuse reflectance-based tumor contrasts for simulations conducted on small tumor models. The lens focal length was 20 mm. The stop size was 4 mm and 6 mm, respectively, when the beam size was 6 mm and 8 mm to generate ring illumination beams. The iris size was the same as the stop size. (B) Fluorescence-based tumor contrasts for simulations conducted on small tumor models. White-field full beam focused illumination was used in fluorescence simulations. The lens focal length was fixed to be 20 mm. Neither a stop nor an iris was used.

Small tumors in mice with a diameter of ∼ 6 mm were commonly recommended for *in vivo* tumor metabolism characterization in flank tumor models because these small tumors retain the actual clinically relevant tumor micro-environment well [37]. Our small tumor models closely mimic the flank small tumor models thereby our findings from this study could be directly applied to future flank tumor model investigations. Comparing the WVF and fluorescence frequency distributions, our studies showed that non-contact fluorescence is more sensitive compared to non-contact diffuse reflectance for small tumor characterizations. However, both diffuse reflectance and fluorescence provided decent tumor contrasts which suggested that our non-contact approach could potentially help characterize small tumors in flank tumor models using non-contact spectroscopy platforms. The early-stage tumor models in our simulations can represent many types of tumor models such as orthotropic tongue cancer models where the tongue tumor is around 3 mm with a depth of ∼0.2 mm. We were not able to use the actual tongue tissue optical properties but subcutaneous tissue optical properties for our simulations due to the limited database for tongue tissue optical properties, which will be explored in our future studies. However, the general trends of tumor contrast changes, optical signal intensities changes, WVF, and fluorescence frequency distributions in our early-stage tumor models should not change significantly even the subcutaneous tissue instead of tongue tissue optical properties were used. Therefore, our findings for the early-stage tumor models in this study could still provide valuable guidelines for future tongue cancer model investigations. Our studies in the early-stage tumor models showed the non-contact approach provided great diffuse reflectance tumor contrast and very high fluorescence tumor contrasts, suggesting our approach has a high sensitivity for early-stage tumor detection, therefore our non-contact approach can be helpful in studying orthotropic tongue tumors in future to provide high detection sensitivity with the additional benefit of no infection concerns.

Our phantom studies for non-contact diffuse reflectance spectroscopy showed that the lens with a shorter focal length (a larger numerical aperture) has a better tumor detection sensitivity compared to the lens with a longer focal length, which is consistent with the simulation results. However, we found that the tumor detection sensitivity was increased significantly only for the lens with a focal length of 25.4 mm but not for other lenses when the light beam focal depth was increased from the tissue surface to the depth under the tumor-like target. The mismatch between our experimental data in Fig. 6(B) and simulation results in Fig. 5(A) is likely because the white

LED light is difficult to collimate and then focused on a small spot inside the tissue. Moreover, the other imaging lenses with longer focal lengths could form a larger focal spot inside the tissue, and this larger focal point inside the tissue may be no longer imaged back to the collection fiber which may potentially lead to decreased performances in tumor detection compared to the lens with a focal length of 25.4 mm. Our fluorescence phantom studies showed that the tumor detection sensitivity was increased when the light beam focal depth was increased for all four lenses, and the lens with a shorter focal length had a better tumor detection sensitivity compared to the lens with a longer focal length. We also demonstrated that dark-field illumination based fluorescence measurements have better tumor detection sensitivity compared to the full beam illumination based fluorescence measurements but with a sacrifice of signal drop (almost by half, data not shown). Overall, our experimental studies using the non-contact optical spectroscopy for both diffuse reflectance and fluorescence measurements on tissue-mimicking solidified the key findings obtained from our simulation studies. In our phantom experiments, one glass tube was used to mimic a tumor-like target. The thickness of the glass tube wall is around 0.3 mm. The glass tube wall thickness may affect the collected intensities from the phantoms, which may consequently affect the absolute tumor contrast values. However, we believe the trends of tumor contrast changes at different configurations should be still the same as those achieved with a glass tumor with a thinner wall. Compared to the actual tumor contrast values, the trends of contrast changes over different configurations will be more useful in terms of guiding system design and optimization.

In our simulation studies, we simulated the homogenous tissue models with a buried tumor-like spherical target, which will more realistically mimic murine subcutaneous tumors compared to the commonly used layered tissue models. To validate our key simulation results in an easy-to-achieve way, we created simple liquid phantoms with a buried cylindrical glass tube (to mimic a tumor target) for phantom studies. As shown in our study, our simple glass tube based phantom can still reasonably help us to solidify the key numerical findings and optimize the system. To better maintain the consistency between the experimental and simulation studies, we will create phantoms with a buried spherical tumor-like target in our future studies. In both simulation and experimental studies, we observed that the lens with a shorter focal length has a better tumor detection sensitivity compared to the lens with a longer focal length for both diffuse reflectance and fluorescence measurements. This is likely because the lens with a shorter focal length had a larger numerical aperture compared to the lens with a longer focal length. As discussed above, a larger numerical aperture will potentially lead to increased tumor detection sensitivity. There could be two potential approaches to achieve a larger numerical aperture for the non-contact setup report in our study. One way is to use lenses with a fixed diameter, but different focal lengths as reported in this manuscript. This is easy to achieve with minimal change on the cage system and one does not need to adjust the initial illumination beam, however, one may need to adjust the distance between the optical elements to ensure the best performance for a new imaging lens. The other way is to use lenses with fixed focal lengths but different diameters. This is feasible to achieve but one needs to adjust the initial illumination beam to increase the numerical aperture of the illumination beams. The tradeoff will need to be made as needed to facilitate the actual experimental requirements.

Our findings showed that one may need to handle the non-contact spectroscopy measurements differently for the detection of superficial tumors and tumors that are in moderately deeper tissue. For superficial tumor measurements, our simulation studies showed that both diffuse reflectance based tumor contrast and fluorescence based contrast reached a plateau when the depth of the focal spot was increased from the superficial layer to the tumor target. These findings suggested that both diffuse reflectance and fluorescence non-contact spectroscopy could provide tumor-sensitive measurements as long as the light focal spot reached the tumor center. For measurements on a tumor that is in moderately deeper tissue, our data showed that both diffuse reflectance-based tumor contrast and fluorescence based contrast increased but did not reach a plateau when the depth of the focal spot was increased from the superficial layer to the tumor target, and these contrasts reached to a plateau when the focal depth went to the region below the tumor target as shown in Fig. 11. Therefore, for deep tumor detection, one may want to focus the beam on the bottom region of the tumor target to get the best tumor detection contrast if the optical signal strength is not a concern. In general, one should use the imaging lens with a short focal length (or large numerical aperture) for both superficial tumor and moderately deep tumor measurements as the lens with a larger numerical aperture always provides better tumor detection contrast. In this study, we explored the feasibility of non-contact optical spectroscopy for tumor-sensitive diffuse reflectance and fluorescence measurements using tissue-mimicking phantoms. In our future study, we will develop our techniques for the quantitative characterization of tumor metabolism and vascular microenvironment on small animals *in vivo*. We will develop a look-up table-based inversion platform for diffuse reflectance spectra data processing to extract vascular parameters, and we will also implement our formerly reported ratio-metric methods [38] for the fluorescence spectra process to provide precise estimates of metabolic parameters.

5. Conclusion

We reported a novel Monte Carlo method to simulate a dark-field non-contact spectroscopy device for both diffuse reflectance and fluorescence measurements on murine subcutaneous tissue models with a spherical tumor-like target. We then numerically investigated the effects of different optical configurations on the diffuse reflectance and fluorescence measurements on the realistic murine subcutaneous tumor models. Our simulation results showed that both the depth of the light focal point and the lens numerical aperture would dramatically affect the system's tumor detection sensitivity. Relying on these findings, we developed and demonstrated a compact non-contact spectroscopy device to perform tumor-sensitive diffuse reflectance and fluorescence measurements on tissue-mimicking phantoms. Our Monte Carlo method can be a useful computational tool for designing non-contact optical spectroscopy systems. Our darkfield optical spectroscopy platform will potentially offer a new way for non-contact optical monitoring of tumor metabolism and vascularization *in vivo* to advance cancer research.

Funding. American Cancer Society (ACS-IRG (19-140-31)); National Institute of General Medical Sciences (R01DE031998, P20GM121327); National Institute of Dental and Craniofacial Research (R01DE031998).

Acknowledgments. This work was supported by NIDCR/NIGMS-R01DE031998 and ACS-IRG (19-140-31). We thank the University of Kentucky Center for Computational Sciences and Information Technology Services Research Computing for their support and use of the Lipscomb Compute Cluster and associated research computing resources. The funders had no role in study design, data collection, analysis, decision to publish, or preparation of the manuscript.

Disclosures. The authors declare that there are no known conflicts of interest related to this article.

Data availability. Data underlying the results presented in this paper are not publicly available at this time but may be obtained from the authors upon reasonable request.

References

1. S. Kim, M. Kim, and J. G. Kim, "Development of simple diffuse optical metabolic spectroscopy for tissue metabolism measurement," Biomed. Opt. Express **10**(6), 2956–2966 (2019).
2. S. Dadgar, J. R. Troncoso, E. R. Siegel, N. M. Curry, R. J. Griffin, R. P. M. Dings, and N. Rajaram, "Spectroscopic investigation of radiation-induced reoxygenation in radiation-resistant tumors," Neoplasia **23**(1), 49–57 (2021).
3. P. M. Diaz, S. V. Jenkins, K. Alhallak, D. Semeniak, R. J. Griffin, R. P. M. Dings, and N. Rajaram, "Quantitative diffuse reflectance spectroscopy of short-term changes in tumor oxygenation after radiation in a matched model of radiation resistance," Biomed. Opt. Express **9**(8), 3794–3804 (2018).
4. C. Zhu, M. Li, T. Vincent, H. L. Martin, B. T. Crouch, A. F. Martinez, M. C. Madonna, G. M. Palmer, M. W. Dewhirst, and N. Ramanujam, "Simultaneous in vivo optical quantification of key metabolic and vascular endpoints reveals tumor metabolic diversity in murine breast tumor models," J Biophotonics **12**, e201800372 (2019).
5. C. Zhu, H. L. Martin, B. T. Crouch, A. F. Martinez, M. Li, G. M. Palmer, M. W. Dewhirst, and N. Ramanujam, "Near-simultaneous quantification of glucose uptake, mitochondrial membrane potential, and vascular parameters in

murine flank tumors using quantitative diffuse reflectance and fluorescence spectroscopy," Biomed. Opt. Express **9**(7), 3399–3412 (2018).

6. D. C. G. De Veld, M. J. H. Witjes, H. J. C. M. Sterenborg, and J. L. N. Roodenburg, "The status of in vivo autofluorescence spectroscopy and imaging for oral oncology," Oral Oncol. **41**(2), 117–131 (2005).
7. C. G. Zhu, S. Chen, C. H. K. Chui, B. K. Tan, and Q. Liu, "Early Prediction of Skin Viability Using Visible Diffuse Reflectance Spectroscopy and Autofluorescence Spectroscopy," Plast Reconstr Surg **134**(2), 240e–247e (2014).
8. K. Radic Shechter, E. Kafkia, K. Zirngibl, S. Gawrzak, A. Alladin, D. Machado, C. Luchtenborg, D. C. Sevin, B. Brugger, K. R. Patil, and M. Jechlinger, "Metabolic memory underlying minimal residual disease in breast cancer," Mol Syst Biol **17**(10), e10141 (2021).
9. A. C. B. Sant'Anna-Silva, G. C. Santos, S. P. C. Campos, A. M. Oliveira Gomes, J. A. Perez-Valencia, and F. D. Rumjanek, "Metabolic Profile of Oral Squamous Carcinoma Cell Lines Relies on a Higher Demand of Lipid Metabolism in Metastatic Cells," Front. Oncol. **8**, 13 (2018).
10. U. Utzinger and R. R. Richards-Kortum, "Fiber optic probes for biomedical optical spectroscopy," J. Biomed. Opt. **8**(1), 121–147 (2003).
11. Y. L. Ti and W. C. Lin, "Effects of probe contact pressure on in vivo optical spectroscopy," Opt. Express **16**(6), 4250–4262 (2008).
12. R. Reif, M. S. Amorosino, K. W. Calabro, O. A'Amar, S. K. Singh, and I. J. Bigioa, "Analysis of changes in reflectance measurements on biological tissues subjected to different probe pressures," J. Biomed. Opt. **13**(1), 010502 (2008).
13. L. A. Lim, B. Nichols, N. Rajaram, and J. W. Tunnell, "Probe pressure effects on human skin diffuse reflectance and fluorescence spectroscopy measurements," J. Biomed. Opt. **16**(1), 011012 (2011).
14. S. Andree, C. Reble, J. Helfmann, I. Gersonde, and G. Illing, "Evaluation of a novel noncontact spectrally and spatially resolved reflectance setup with continuously variable source-detector separation using silicone phantoms," J. Biomed. Opt. **15**(6), 067009 (2010).
15. S. F. Bish, N. Rajaram, B. Nichols, and J. W. Tunnel, "Development of a noncontact diffuse optical spectroscopy probe for measuring tissue optical properties," J. Biomed. Opt **16**(12), 120505 (2011).
16. M. Mazurenka, A. Jelzow, H. Wabnitz, D. Contini, L. Spinelli, A. Pifferi, R. Cubeddu, A. Dalla Mora, A. Tosi, F. Zappa, and R. Macdonald, "Non-contact time-resolved diffuse reflectance imaging at null source-detector separation," Opt. Express **20**(1), 283–290 (2012).
17. S. Y. Lee and M. A. Mycek, "Hybrid Monte Carlo simulation with ray tracing for fluorescence measurements in turbid media," Opt. Lett. **43**(16), 3846–3849 (2018).
18. C. G. Zhu, Y. H. Ong, and Q. Liu, "Multifocal noncontact color imaging for depth-sensitive fluorescence measurements of epithelial cancer," Opt. Lett. **39**(11), 3250–3253 (2014).
19. F. Hu, R. Morhard, H. A. Murphy, C. Zhu, and N. Ramanujam, "Dark field optical imaging reveals vascular changes in an inducible hamster cheek pouch model during carcinogenesis," Biomed. Opt. Express **7**(9), 3247–3261 (2016).
20. C. G. Zhu and Q. Liu, "Numerical investigation of lens based setup for depth sensitive diffuse reflectance measurements in an epithelial cancer model," Opt. Express **20**(28), 29807–29822 (2012).
21. L. H. V. Wang and G. Liang, "Absorption distribution of an optical beam focused into a turbid medium," Appl. Opt. **38**(22), 4951–4958 (1999).
22. T. S. Evan Carrico and C. Zhu, "Numerical investigation of depth-sensitive diffuse reflectance and fluorescence measurements on murine subcutaneous tissue with growing solid tumors," Biomed. Opt. Express **11**(11), 6311–6323 (2020).
23. Q. Liu, C. F. Zhu, and N. Ramanujam, "Experimental validation of Monte Carlo modeling of fluorescence in tissues in the UV-visible spectrum," J. Biomed. Opt. **8**(2), 223–236 (2003).
24. Caigang Zhu and Q. Liu, "Validity of the semi-infinite tumor model in tissue optics: a Monte Carlo study," in *2010 Photonics Global Conference (PGC)* (IEEE, 2010), pp. pp. 1–4.
25. M. J. McShane, S. Rastegar, M. Pishko, and G. L. Cote, "Monte Carlo modeling for implantable fluorescent analyte sensors," IEEE Trans. Biomed. Eng. **47**(5), 624–632 (2000).
26. R. J. Crilly, W. F. Cheong, B. Wilson, and J. R. Spears, "Forward-adjoint fluorescence model: Monte Carlo integration and experimental validation," Appl. Opt. **36**(25), 6513–6519 (1997).
27. K. Vishwanath, B. Pogue, and M. A. Mycek, "Quantitative fluorescence lifetime spectroscopy in turbid media: comparison of theoretical, experimental and computational methods," Phys. Med. Biol. **47**(18), 3387–3405 (2002).
28. D. Y. Churmakov, I. V. Meglinski, and D. A. Greenhalgh, "Amending of fluorescence sensor signal localization in human skin by matching of the refractive index," J. Biomed. Opt. **9**(2), 339–346 (2004).
29. J. Swartling, A. Pifferi, A. M. Enejder, and S. Andersson-Engels, "Accelerated Monte Carlo models to simulate fluorescence spectra from layered tissues," J. Opt. Soc. Am. A **20**(4), 714–727 (2003).
30. S. K. Chang, D. Arifler, R. Drezek, M. Follen, and R. Richards-Kortum, "Analytical model to describe fluorescence spectra of normal and preneoplastic epithelial tissue: comparison with Monte Carlo simulations and clinical measurements," J. Biomed. Opt. **9**(3), 511–522 (2004).
31. C. P. Sabino, A. M. Deana, T. M. Yoshimura, D. F. da Silva, C. M. Franca, M. R. Hamblin, and M. S. Ribeiro, "The optical properties of mouse skin in the visible and near infrared spectral regions," J. Photochem. Photobiol., B **160**, 72–78 (2016).

32. G. Greening, A. Mundo, N. Rajaram, and T. J. Muldoon, "Sampling depth of a diffuse reflectance spectroscopy probe for in-vivo physiological quantification of murine subcutaneous tumor allografts," J. Biomed. Opt. **23**(08), 1 (2018).
33. Q. Liu and N. Ramanujam, "Sequential estimation of optical properties of a two-layered epithelial tissue model from depth-resolved ultraviolet-visible diffuse reflectance spectra," Appl. Opt. **45**(19), 4776–4790 (2006).
34. S. H. Tseng, C. K. Hayakawa, J. Spanier, and A. J. Durkin, "Determination of optical properties of superficial volumes of layered tissue phantoms," IEEE Trans. Biomed. Eng. **55**(1), 335–339 (2008).
35. R. Hennessy, W. Goth, M. Sharma, M. K. Markey, and J. W. Tunnell, "Effect of probe geometry and optical properties on the sampling depth for diffuse reflectance spectroscopy," J. Biomed. Opt **19**(10), 107002 (2014).
36. M. Z. Hasan, J. Yan, Z. C. Yi, M. O. Korfhage, S. Tong, and C. G. Zhu, "Low-Cost Compact Optical Spectroscopy and Novel Spectroscopic Algorithm for Point-of-Care Real-Time Monitoring of Nanoparticle Delivery in Biological Tissue Models," IEEE J. Select. Topics Quantum Electron. **29**, 1–8 (2023).
37. I. Serganova, A. Rizwan, X. Ni, S. B. Thakur, J. Vider, J. Russell, R. Blasberg, and J. A. Koutcher, "Metabolic imaging: a link between lactate dehydrogenase A, lactate, and tumor phenotype," Clin. Cancer Res. **17**(19), 6250–6261 (2011).
38. T. Sun and C. Zhu, "Empirical method for rapid quantification of intrinsic fluorescence signals of key metabolic probes from optical spectra measured on tissue-mimicking turbid medium," J. Biomed. Opt. **26**(04), 045001 (2021).